nature methods

SUPPLEMENTARY INFORMATION

https://doi.org/10.1038/s41592-018-0180-2

In the format provided by the authors and unedited.

# The hit-and-return system enables efficient time-resolved serial synchrotron crystallography

**Eike C. Schulz[1,11], Pedram Mehrabi[1,11], Henrike M. Müller-Werkmeister[1,2,11], Friedjof Tellkamp[3], Ajay Jha[1], William Stuart[1], Elke Persch[4], Raoul De Gasparo[4], François Diederich[4], Emil F. Pai[5,6,7,8]* and R. J. Dwayne Miller[1,9,10]***

[1]Department for Atomically Resolved Dynamics, Max Planck Institute for Structure and Dynamics of Matter, Hamburg, Germany. [2]Physical Chemistry, Institute of Chemistry, University of Potsdam, Potsdam-Golm, Germany. [3]Scientific Support Unit Machine Physics, Max Planck Institute for Structure and Dynamics of Matter, Hamburg, Germany. [4]Laboratorium für Organische Chemie, ETH Zürich, Zürich, Switzerland. [5]Department of Biochemistry, University of Toronto, Toronto, Ontario, Canada. [6]Department of Medical Biophysics, University of Toronto, Toronto, Ontario, Canada. [7]Department of Molecular Genetics, University of Toronto, Toronto, Ontario, Canada. [8]The Campbell Family Cancer Research Institute, Ontario Cancer Institute, Toronto, Ontario, Canada. [9]Departments of Chemistry and Physics, University of Toronto, Toronto, Ontario, Canada. [10]Department of Physics, Centre for Ultrafast Imaging, University of Hamburg, Hamburg, Germany. [11]These authors contributed equally: Eike C. Schulz, Pedram Mehrabi, Henrike M. Müller-Werkmeister.
*e-mail: emil.pai@utoronto.ca; dwayne.miller@mpsd.mpg.de

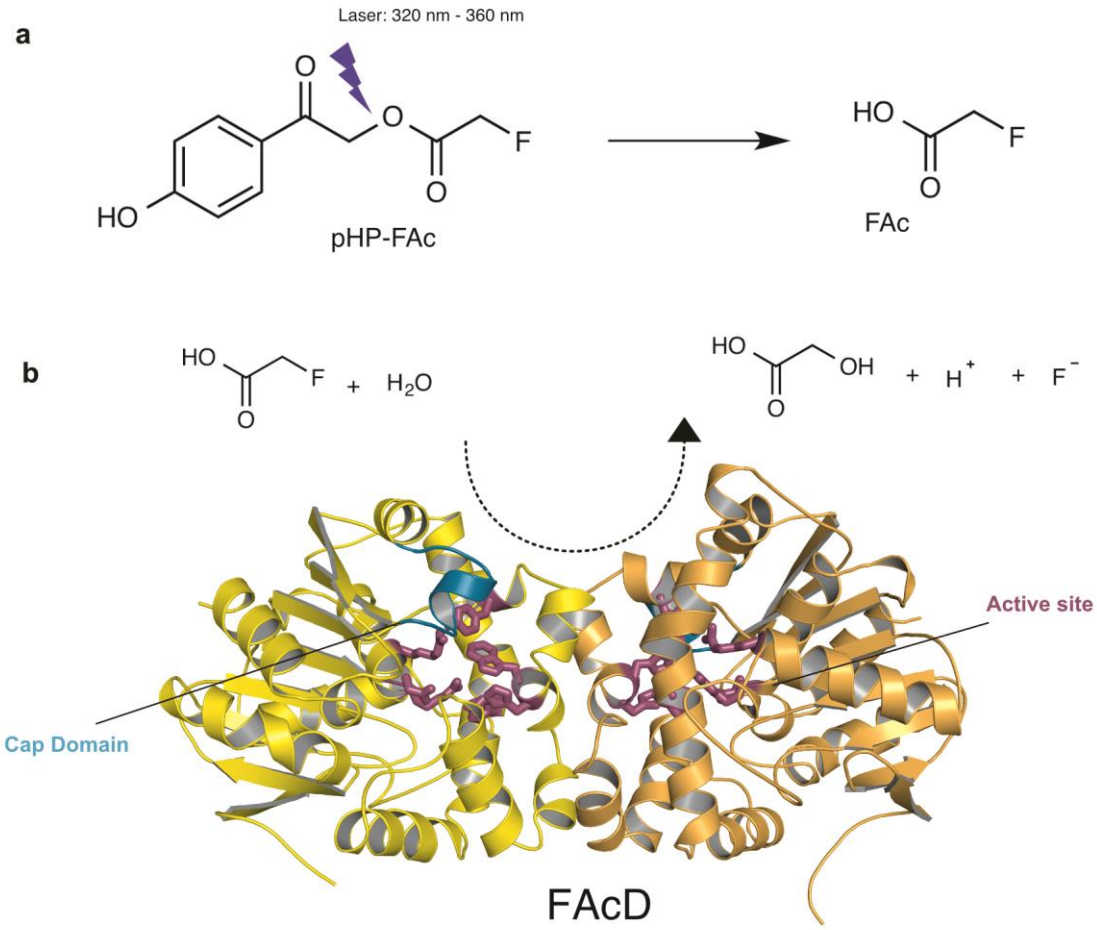


**Supplementary Figure 1**

Homodimeric fluoroacetate dehalogenase and photolytic generation of its substrate fluoroacetate.

**a**, The photocaged substrate for FAcD pHP-FAc is sensitive to photolysis initiated by UV light pulses with a wavelength between 320 nm and 360 nm. Cleavage of the phenol group releases FAcD's substrate fluroacetate. **b**, A cartoon representation of homodimeric FAcD with the backbone of subunit A in yellow and subunit B in orange. The location of the cap domain (cyan) and the positions of the active site residues (purple) are indicated.

a

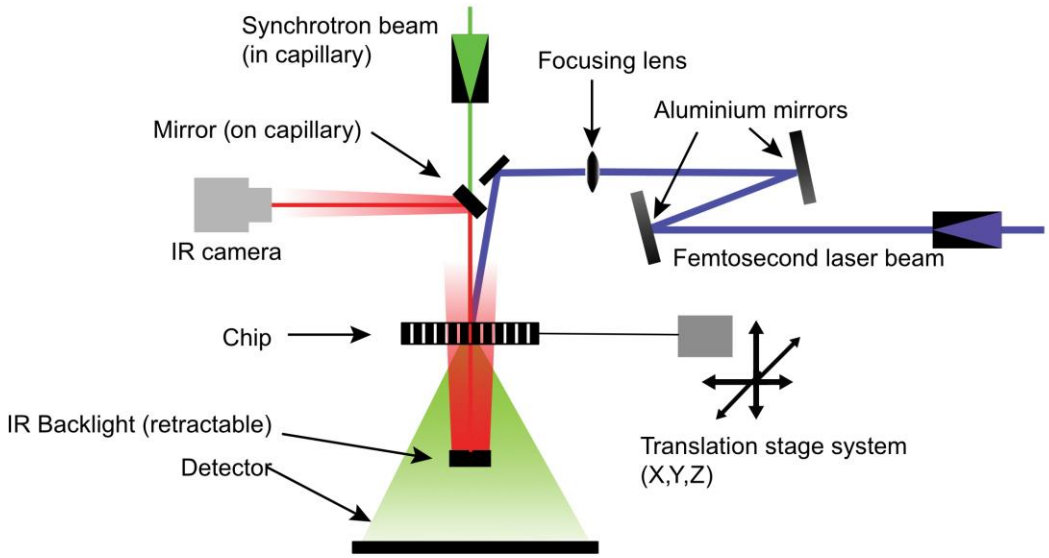
Synchrotron beam
(in capillary)
Focusing lens
Aluminium mirrors
Mirror (on capillary)
IR camera
Femtosecond laser beam
Chip
IR Backlight (retractable)
Detector
Translation stage system
(X,Y,Z)

b

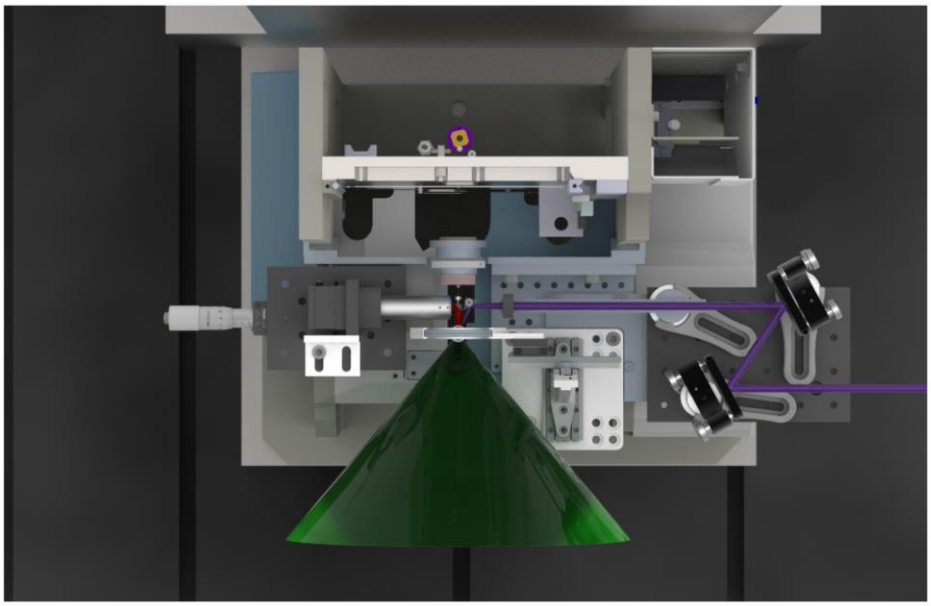

c

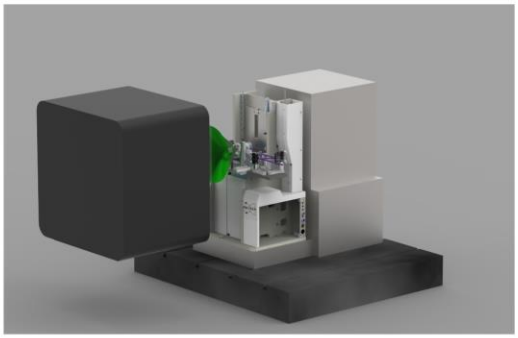

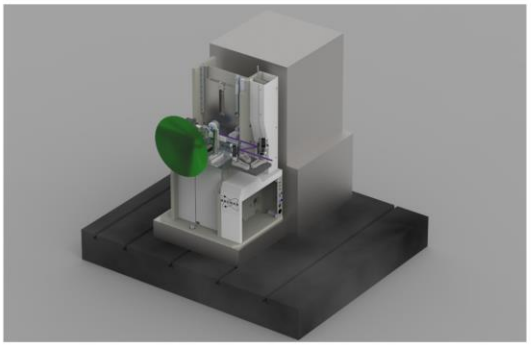

**Supplementary Figure 2**

End station design.

**a**, Top-down schematic of a typical light-triggered SSX arrangement. The chip can be viewed from an IR camera using a mirror mounted on a capillary which is illuminated via a retractable IR backlight. Alignment and chip movement are done via the translation stage system. Samples on the chip are pumped via a femtosecond laser and probed via the X-ray beam; the diffraction cone is represented in green. **b**, CAD representation of **a**. **c**, A CAD representation of the end station with and without the detector. The diffraction cone is represented in green.

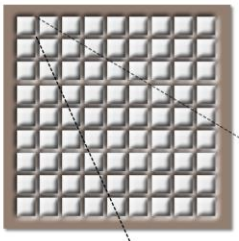

chip gen. 1

-compartments: 9 x 9 = 81
-features: 12 x 12 = 144
-total features: 11,664
-pitch: 125 $\mu$m

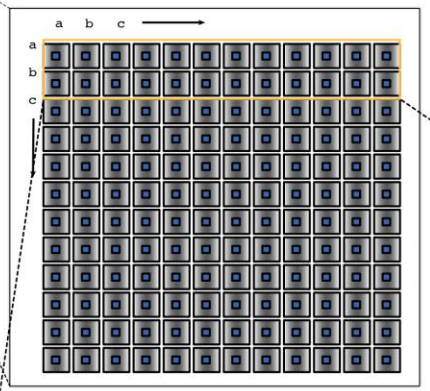


compartment

**I.** **X-ray exposure = $t_0$ image** (reference)

**II.** **Laser pulse** (pump)

**III.** Chip moves to next feature. Repeat sequence I-III for (`aa...bl`)

**IV.** Chip moves back to initial position (`aa`)

**V.** **X-ray exposures** (probe) after time for chip motion between (`aa...bl`) = **$t_{delay}$ image**

**VI.** Repeat sequence I-V from feature `ca` onwards ...

**Pump-run (Hit)**

- 1st exposure
- diffraction data for $t_0$
- laser pump

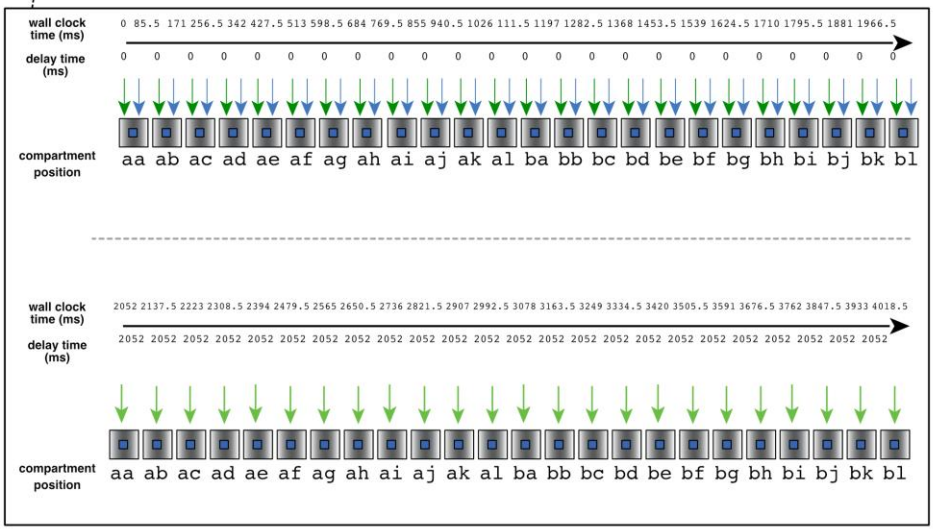


**Probe-run (Return)**

- 2nd exposure
- diffraction data for $t_{delay}$

## Hit-and-Return reduces the cumulative data collection time

In Hit-and-Return the data collection time is optimized by reference data collection ($t_0$) and reaction initiation (pump) of further crystals during the delay time. After the delay time the system returns to the initial position to collect the probe data. The delay time is defined by variable parameters the pitch of the features, the translation time, the X-ray exposure and the Laser exposure all of which are summarized in a single Hit-and-Return number. The longer the delay time should be the more features can be pumped before a probe run the higher the Hit-and-Return number. By contrast, using sequential delays the delay times would accumulate to much longer data-collection times. This effect is more pronounced for longer delay times.

**How long sequential delays would take**:

2000 ms delay§ + 43.5 ms chip translation =

2043.5 ms / 1 crystal * 11,664 features =

**1 Chip = 397.3 min ~ 6.6 h**

**Hit-and-Return delays**:

24 * (43.5 ms chip translation + 40 ms exposure period$ + 2 ms laser excitation) = 2052 ms

2* 2052 ms / 24 crystals * 11,664 features = 171

**1 Chip = 33.27 min ~ 0.5 h**

§ For sequential delays the exposure period and laser excitation would be included in the delay time

$ exposure period = 15ms X-ray exposure plus detector opening time

**Supplementary Figure 3**

The HARE approach with chip gen. 1.

A representation of a single compartment on the chip with 12 × 12 features. X-ray pulses are depicted in green, and laser pulses are shown in blue. In order to have a large number of valid HARE times, it is most efficient for the number of features per compartment row and column to be a highly composite number (e.g., 12). Longer times than a HARE value of 12 would therefore need to be certain multiples of 12 (e.g., 24, 36, 48, etc.). Data collection for an HARE of 24 would be as follows: Starting from row a, the first feature in the first column (aa) is exposed to an X-ray pulse and a subsequent dark image is recorded. Immediately following the X-ray pulse the sample is pumped with the femtosecond laser for $t = 0$. This procedure is repeated for a total of 24 features. After pumping of the 24 features, the stages move back to their starting positions. The same 24 features are then re-probed with X-rays after a delay time matching the total time for probe-pumping of the 24 features. For every probed feature on the chip, the resulting data include both a dark image and an exposed image with a corresponding delay dependent on the HARE number.

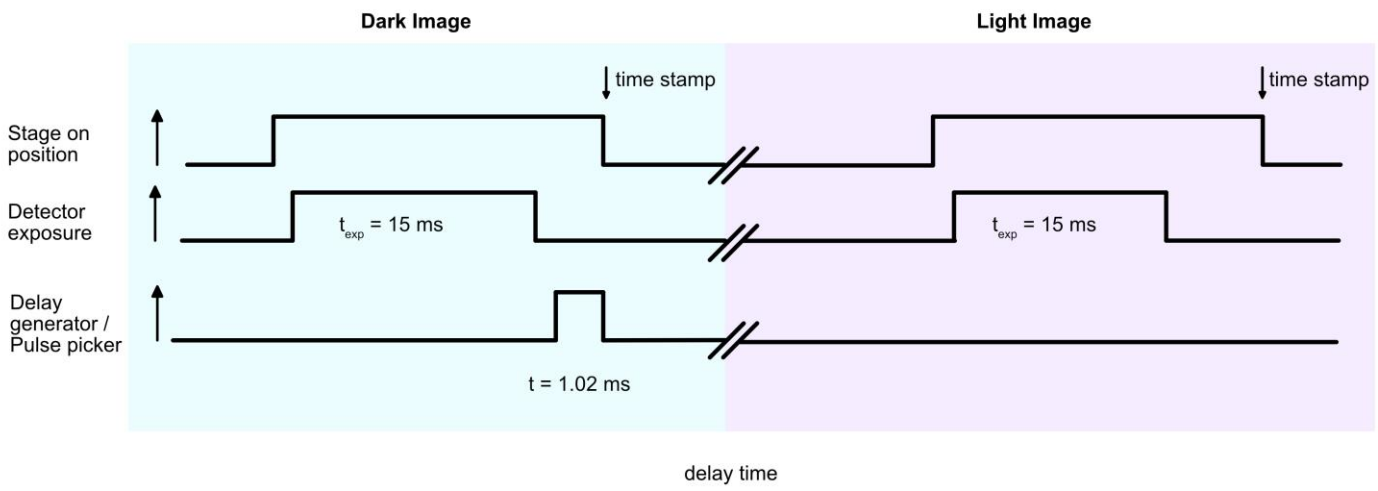


**Supplementary Figure 4**

Pulse sequence.

The pulse sequence plot shows the relative on and off times of the various instruments of our setup. Initially a dark image is taken: (1) the stage moves into position, (2) the detector is set to exposure mode, and (3) after a dark image is acquired a TTL pulse triggers the laser. After the laser pulse there is a delay corresponding to the HARE number, during which further images are acquired. After the delay the stages move back to their original position and the sequence is repeated without laser excitation.

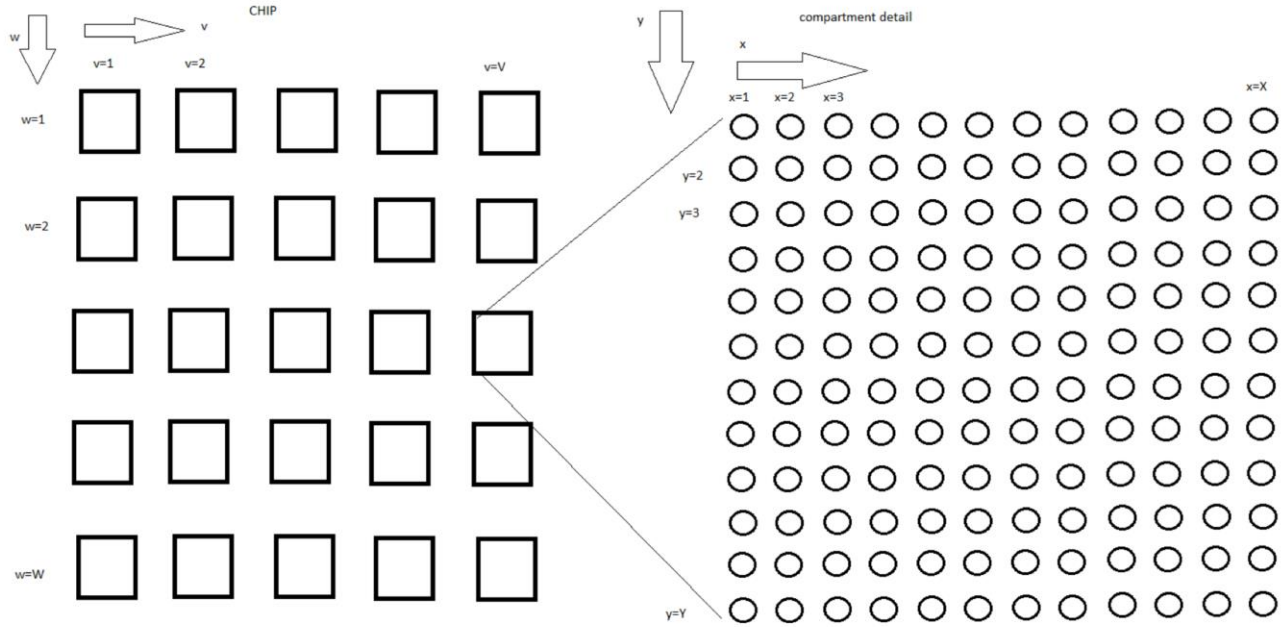


**Supplementary Figure 5**

Description of the HARE formalism.

Let the coordinates (*v*, *w*) denote the index of the compartment in the horizontal and vertical directions, and let (*x*, *y*) be the index of the feature inside the compartment. With $N_v$ and $N_w$ as the number of compartments in the horizontal and vertical directions, $N_x$ and $N_y$ as the number of features per compartment in the horizontal and vertical directions, and *C* as the HARE constant, the coordinates can be determined by

$$v = \frac{i-1}{2N_f} \bmod N_v + 1$$

$$w = \frac{i-1}{2N_v N_f} + 1$$

$$x = \frac{j}{2C} C \bmod N_x + \mathrm{j} \bmod \min\left(N_x,\ C\right) + 1$$

$$y = \frac{j}{2C}\frac{C}{N_x} \bmod N_x + \frac{j}{N_x} \bmod \frac{C}{N_x} + 1$$

with $x$ as the floor function, $N_c = N_v N_w$, $N_f = N_x N_y$, $j = (i - 1) \bmod 2N_f$ and $i$ as the exposure index ranging from 1 to the total number of exposures $2N_c N_f$. These four equations apply if $C|N_x$ for $C \leq N_x$ or if $N_x|C \wedge C|N_f$ otherwise. Laser excitation takes place if $(i - 1) \bmod 2C < C$. In order to have a high number of valid HARE times, it is helpful to choose $N_x$ and $N_y$ as highly composite numbers. The number of possible HARE times can be calculated by $\sigma_0(N_x) + \sigma_0(N_y) - 1$, where $\sigma_x(n)$ is the divisor function.

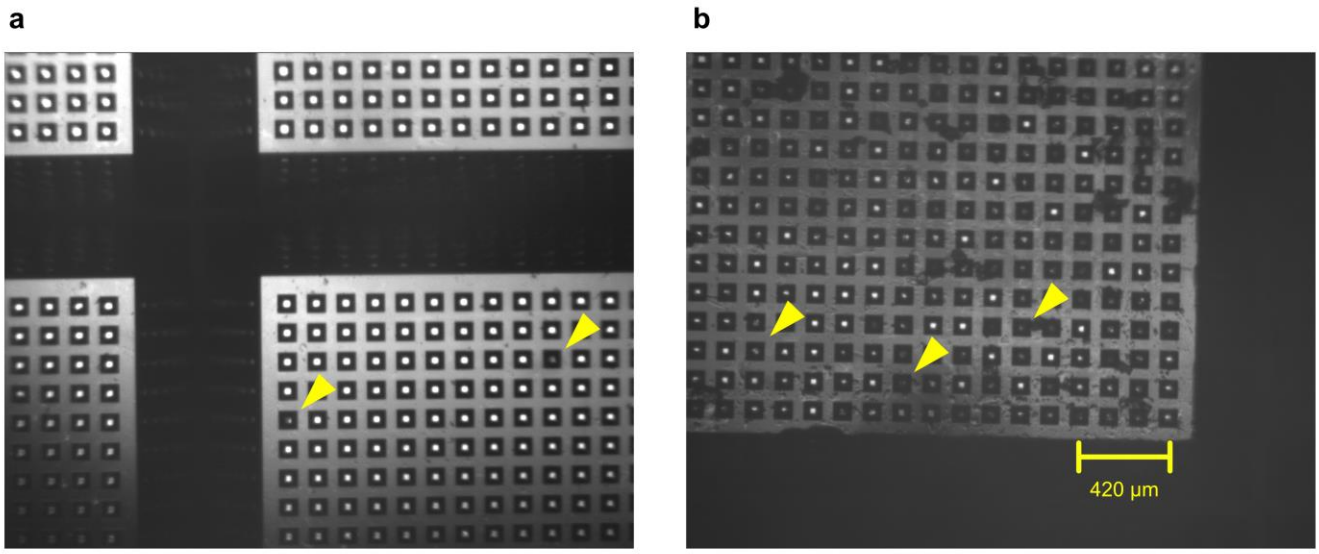


**Supplementary Figure 6**

Infrared images of the chip.

**a**, An empty chip is shown as a control. The yellow arrows point out underdeveloped features, which appear semi-transparent in the IR light. **b**, Loaded chip with yellow arrows representing crystals sitting in the features of the chip. Crystals sitting inside of the features can be clearly distinguished from crystals on its surface and from empty features.

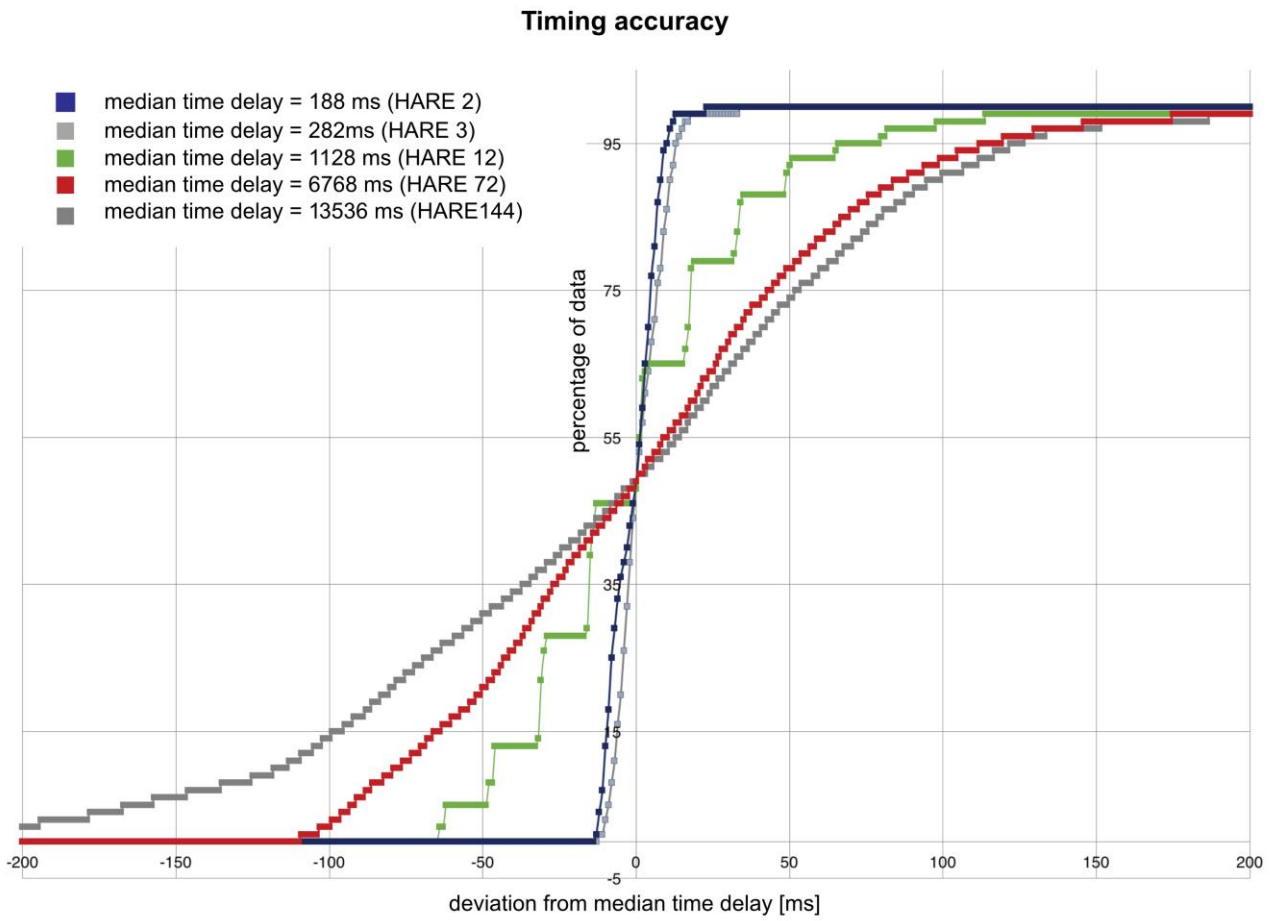


**Supplementary Figure 7**

Cumulative distribution function for time delays.

The plot represents the deviation in milliseconds for five representative HARE values (2, 3, 12, 72 and 144) from their respective median values. The individual median values for each of the five HARE times are set to 0 ms for comparison in the plot. Although the greatest HARE values have the largest deviation from the median, the total percent difference is comparatively small. Data were derived from the total features of a randomly selected chip per time point.

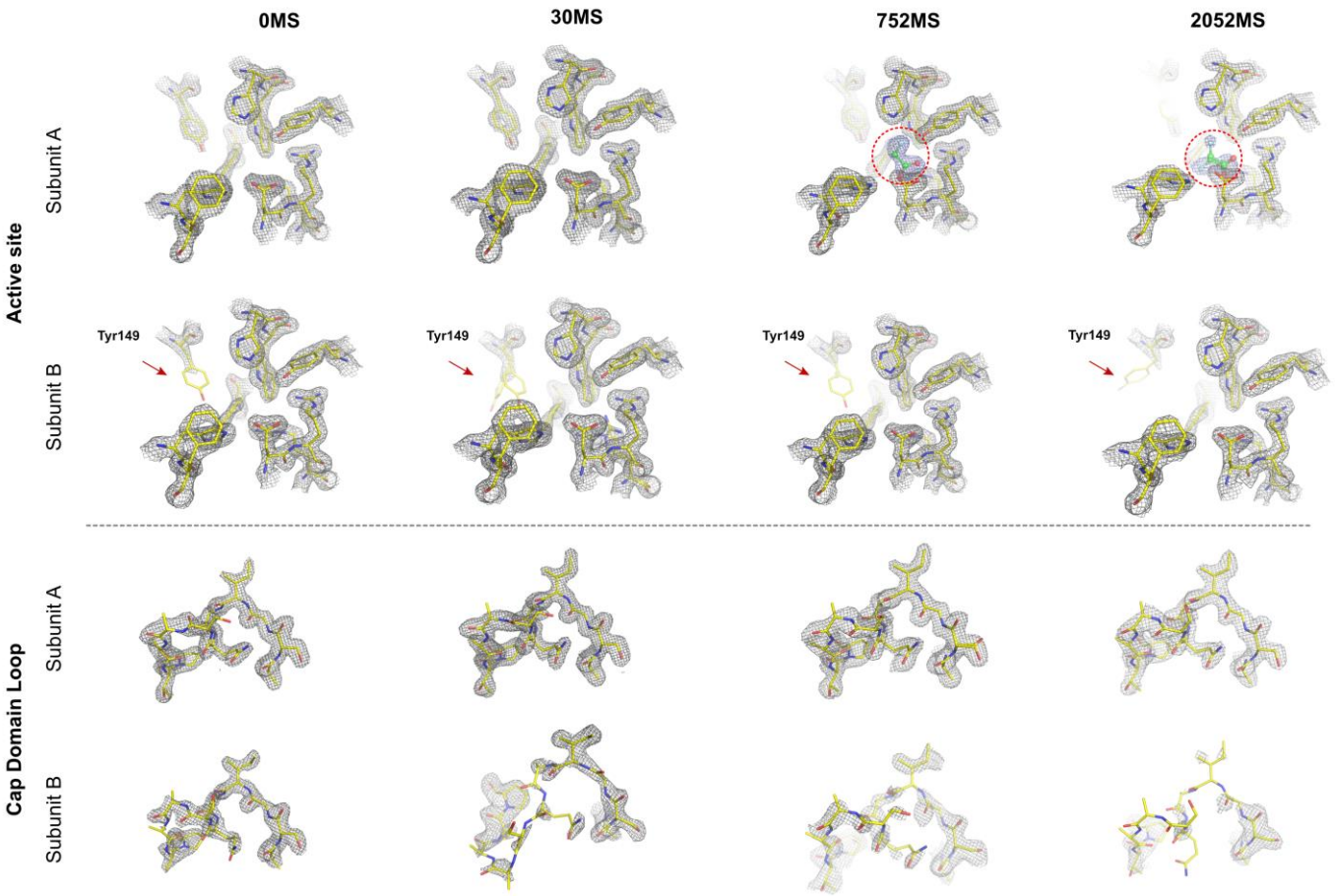


**Supplementary Figure 8**

Absolute value END-RAPID maps.

FAcD electron density changes as a function of time. All electron density maps are represented as absolute value END-RAPID maps at a value of 0.3e $A^{-3}$ σ. The electron density for the bound ligand in active site A is highlighted by a red circle. The flexible side chain of Tyr149 is indicated by a red arrow. The absolute value maps allow for quantitative comparability of the structures by placing all the different time points on an absolute scale, thereby emphasizing that the reduction of the electron observed in the cap domain is a result of enzymatic turnover and not an artifact originating from σ offset of the maps. However, the observed differences recapitulate the changes in the electron density seen in the POLDER-OMIT maps.

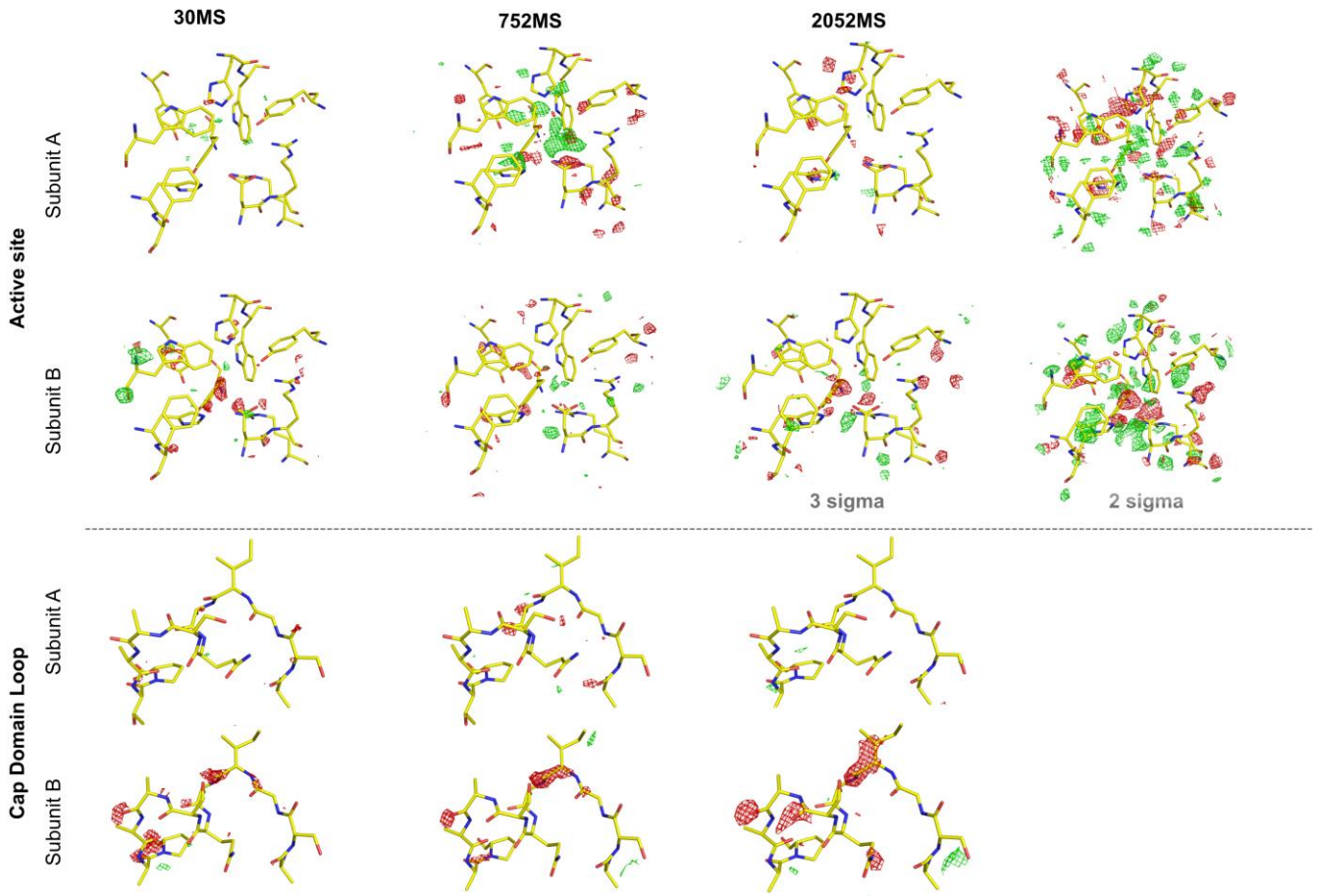


**Supplementary Figure 9**

$F_{obs}$–$F_{obs}$ difference density maps.

Difference electron density maps, shown in green (positive) and red (negative), of the 30-ms, 752-ms and 2,052-ms structures compared with the 0-ms structure contoured at 3.0σ. There are few to no differences in the active sites of the 30-ms structure. There is a large influx of density in subunit A of the 752-ms structure, which is indicative of the Michaelis complex. Differences in the active site in the 2,052-ms structure are readily observed only when the contour levels are decreased to 2.0σ. This is probably due to insufficient signal to noise. Whereas the cap domain in subunit A remains constant over time points, the cap domain in subunit B shows a consistent trend of increased dynamics as indicated by the increase in negative density as the reaction proceeds.

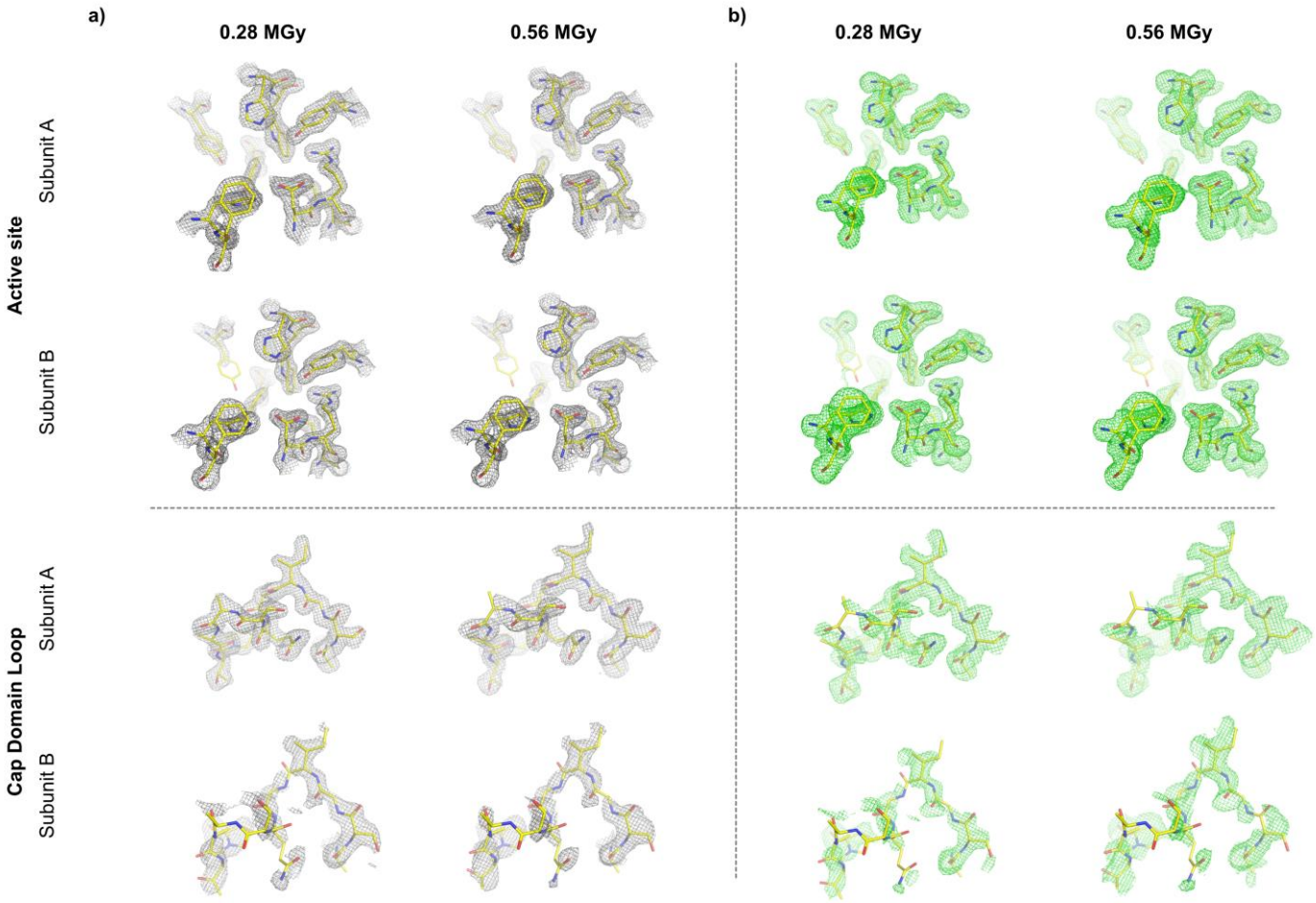


**Supplementary Figure 10**

Radiation damage.

The figure shows absolute value END-RAPID (**a**) and POLDER-OMIT (**b**) maps for a structure exposed to 0.28 MGy and 0.56 Mgy, respectively. The maps clearly show equivalent electron density for the active site and the cap-domain loop in both subunits, irrespective of the cumulative radiation dose. This not only shows the radiation insensitivity of the enzyme but also demonstrates that the disordering of the cap-domain loop is associated with enzymatic turnover and not induced by radiation damage.

a)

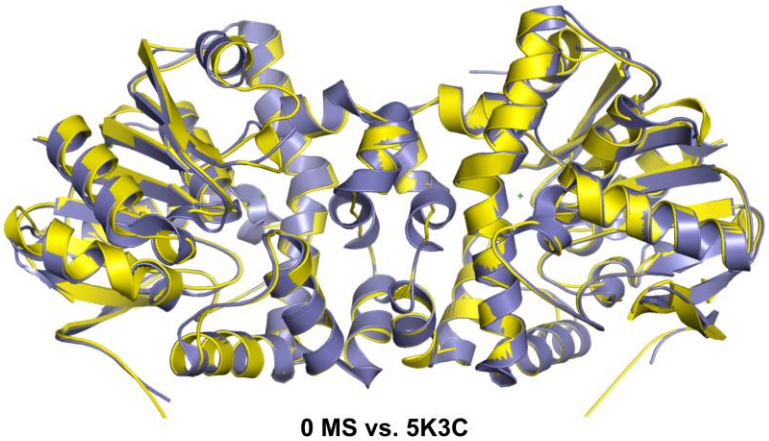

0 MS vs. 5K3C

r.m.s.d.: 0.42 Å

b)

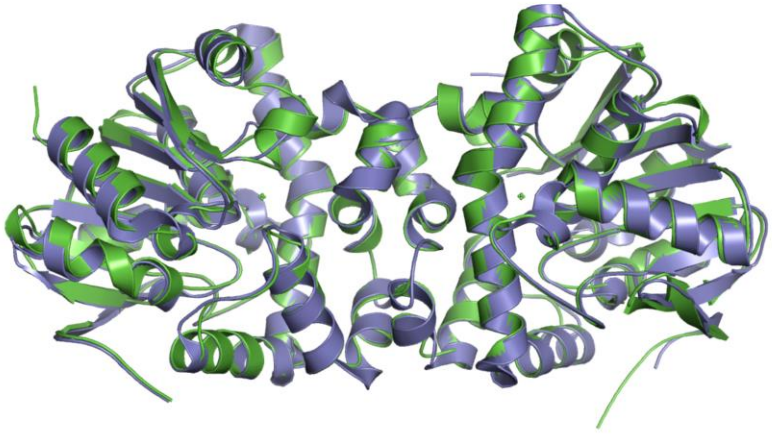

2052 MS vs. 5K3C

r.m.s.d.: 0.47 Å

c)

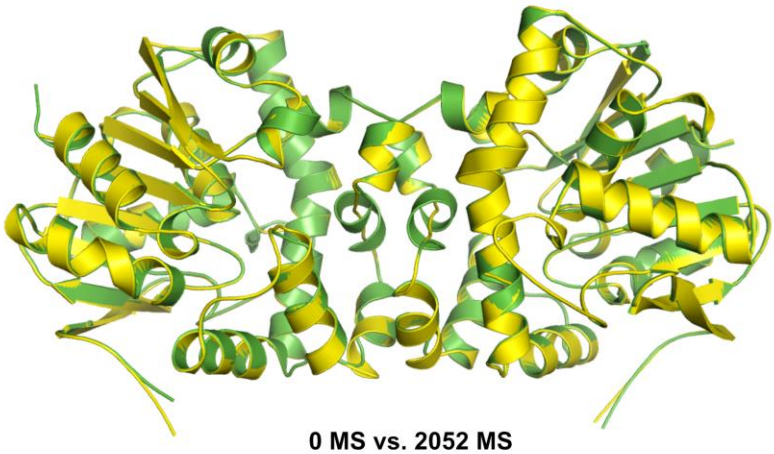

0 MS vs. 2052 MS

r.m.s.d.: 0.16 Å

**Supplementary Figure 11**

Structure comparison.

The figure shows cartoon representations of FAcD with the 0-ms structure in yellow, the previously solved structure PDB 5K3C in purple and the 2,052-ms structure in green. The superpositioning reveals minimal r.m.s. deviation differences between the respective time-point structures and the previously solved cryo-structure (**a**, **b**) and even smaller differences between the two time-point structures (**c**).

# Supplementary Results

### Comparison of sequential and HARE time delays

For comparison a single chip using sequential delays would take ~4.7 h (752 ms delay[§] + 72 ms chip translation = 824 ms / crystal * 20,736 features = 284.8 min) while the cumulative data collection takes only ~1h using the HARE delays (8* (72 ms chip translation + 20 ms exposure period + 2 ms laser excitation) = 752 ms / 8 crystals * 20,736 features = 64.9 min). [§]For sequential delays the exposure period and laser excitation would be included in the delay time. [$]exposure period = 15 ms X-ray exposure plus detector opening time.

### Accuracy of the timing

To assess the timing accuracy of our setup we have plotted distribution functions of five different time delays for a whole chip (Supplementary Fig. 7). The plot shows the percentage of diffraction images with their deviation in ms from the median. The time delays shown are HARE 2 = 188 ms, HARE 3 = 282 ms, HARE 12 = 1128 ms, HARE 72 = 6768 ms and HARE 144 = 13536 ms. The plot shows the reproducibility of the time delay. For a time delay of 188 ms and 282 ms the deviation from the median value is on the order of +/- 5ms, corresponding to an error of +/- 3.5 % and 2.6 %, respectively. For long time delays the absolute deviation is larger, but the relative error is small, i.e. for the time delay of 13536 ms the maximum deviation from the median value is - 200 ms/ + 150 ms, corresponding to a relative error of max. -1.7 %. By using more refined algorithms and modified motion control electronics one could achieve higher timing accuracies, but with the drawback of a reduced measurement rate. By contrast to liquid sample injection approaches, there is a trade-off between increasing the velocity (>>30 Hz) of the translation stages to its positional accuracy[1]. Importantly, however, the accuracy of the individual time-points would not be affected.

### Radiation Damage

To address the concern of X-ray damage, we recorded two dark structures (i.e. without laser-pulses), after 1 (0.28 MGy) and 2 (0.56 MGy) X-ray pulses, respectively. These structures do not show any detectable differences between each other. They also do not show reduced electron density for the cap-domain loop, further substantiating that the reduced electron density we see for this region in the 752

ms and 2052 ms time-points is clearly associated to its biological function (**Supplementary Fig. 10**). Conversely, the longer the reaction of the enzyme is allowed to progress the more structural changes can be observed, while the cumulative dose never exceeds 0.56 and 0.74 MGy, respectively. In addition, these structural changes fully parallel those of our previous static studies, where we can observe that the disordering of the cap-domain loop is associated with substrate turnover by FAcD (**Supplementary Fig. 11**)[2, 3].

## Supplementary Discussion

To truly understand how proteins function one requires a detailed examination of all operating time scales. TRX is one of the few methods available that provide access to the dynamics of biomolecular reactions in structural terms. Since the advent of XFEL sources this relatively well established technique has regained popularity [4-7]. Serial femtosecond crystallography (SFX) re-established this technique as a large series of single-shot experiments, greatly facilitating data collection and providing access to non-reversible reactions in time-resolved experiments (TR-SFX). The problem has been that to date these studies have been restricted to the use of large crystals and conventional data collection methods limiting the scope of potential experiments due to both limited supply of sufficient quality crystals and X-ray damage considerations [5, 6, 8, 9]. Only very few of the TRX studies do not rely on reversible, light induced systems and radiation damage of the sample often proves to be a serious problem. With the advent of X-ray free-electron laser (XFEL) sources TRX has re-gained popularity. At XFELs TRX is performed as a series of single-shot experiments in a pump-probe fashion. To this end, a large variety of sample delivery methods has been developed to serve the need to inject thousands to millions of individual micro-crystals into the X-ray beam[10-20].

Since the first demonstration of serial femtosecond crystallography (SFX) many different protein systems have been studied[21-24]. These involved the carbon-monoxide release from myoglobin, structural changes within photosystem I-ferredoxin, the oxygen evolving complex in photosystem II and the trans-cis conformational transition in photoactive yellow protein (PYP)[25-31]. All these systems have in common that they employed liquid jet injectors, were photo-triggered and the majority of time points were in the picosecond or longer domain. To expand the number of accessible systems and address non-photoinducible enzymes three similar *in-situ* mixing methods were described recently[12, 32-34]. Nevertheless, similar to previous approaches these methods focussed on fast time-points, albeit slower time-points should be accessible[32].

Data collection in serial femtosecond crystallography (SFX) is based on the *diffraction-before-destruction* principle [22, 35]. In SFX the diffraction information can be captured on femtosecond time scales based on the durations of the laser excitation pulse, the X-ray probe pulse, and relative time delay between the pump and probe. This has two advantages: the first is the ultra-short time of the

probe pulses that even enable the capture of intermediates of ultra-fast processes such as bond-vibration, base-wobbling, global twisting and side-chain rotations[36]. The second advantage is the absence of most radiation damage effects, as the diffraction process and thereby data generation stops well before major secondary damage processes commence. In SFX, data collection is thus based on the recording of thousands of still images of individual crystals, where every crystal is exposed to a high-intensity X-ray pulse only once. For studying ultrafast time-resolved structural changes in biological macromolecular systems involving 10 micron scale crystals, XFEL sources are currently the only tools available that provide a temporal resolution on the femtosecond to nanosecond timescale. However, serial crystallography is not limited to XFELS but can also be conducted at synchrotron sources (serial synchrotron crystallography - SSX). The general principle in SSX is largely the same as in SFX, with the advantage of much better availability of SSX beamtime generating increased potential for structural biology applications.

**Sample-transfer and reaction initiation systems**

In addition to optically triggered systems the "mix-and-inject" approach was introduced for XFELs[33, 34]. Here the crystal suspension and the ligand solution are transferred through a T-junction mixer before ejection into the XFEL beam. One of the current limitations with this approach lies in the population mixing that can result from the laminar flow in the capillary[12]. However, more importantly the liquid jet technology does not allow to address time-points below 30 ms or higher than 2000 ms. Modifications of these time-ranges would require changes to the flow-rate, and major hardware alterations to the device [33]. In comparison to liquid jet injectors the tape-drive technology appears to bear higher potential for time-resolved studies on biologically relevant time-scales. At the moment, two different approaches have been described: Based on XFEL experiments, the "drop-on-tape" approach was described also offering time ranges with higher temporal flexibility than liquid-jet injectors [12]. However, different time-delays require modifications to the laser setup or the transfer speed of the belt [12]. For synchrotron radiation experiments, the "mix-and-diffuse" approach similar to "mix-and-inject" system, was described [32, 34]. However, while the "mix-and-inject system" cannot address time-points longer than 2 s, the "mix-and-diffuse system" was reported to be unable to

measure time points shorter than 2 s or longer than 50 s without significant hardware revision. In addition, the tape-drive system suffers from higher background scattering due to larger path length for the X-rays through large droplets (~280 µm) and polymer scattering from the belt material. With increasing time-delays background scattering from dehydrating droplets as well as PEG interactions with helium could become problematic.

Conversely, in our system most of the solvent is removed when the crystals are fixed to the chip. In contrast to our approach, it currently appears difficult for the above mentioned systems to quickly change between various time delays. By contrast our setup requires no hardware modifications only quick changes in input parameters to sample time-points ranging from a few milliseconds to several minutes if large portions of the chip are sampled. Additionally, our setup provides the advantage of obtaining a dark-reference pattern for every crystal measured, which can potentially be turned into a novel data-analysis method [37]. However, the most substantial advantage of our HARE approach is that it provides a solution for sampling very slow time-points with comparable throughput to that of fast time-points, in contrast especially to the tape drive approach.

### Radiation Damage

Unfortunately, there are currently only very few studies addressing radiation damage for room-temperature diffraction measurements and none that would specifically address this question for serial crystallography. Important differences for room temperature data collection are the *rate* of diffusion of free radical through the crystal lattice, the quenching of radicals by solvent molecules and most importantly free-radical recombination, which is ~$10^7$ times faster at room temperature than under cryo conditions[38]. Here, each crystal was probed with X-rays of the indicated energy (**Supplementary Table 1, 2**). For those time-points that were recorded using the HARE approach (752 ms, 2052 ms) each crystal was exposed twice, hence the total dose was 0.56 MGy and 0.74 MGy, respectively depending on the beamline. The Garman-limit for a cryo-cooled crystal lies at 43 MGy, while for room-temperature crystals the old Blake and Phillips value of 0.59 MGy is often quoted [39, 40]. Our cumulative dose is either below this conservative level or only slightly exceeds this value. However, recently an inverse dose-rate effect was demonstrated for room-temperature data showing a positive

linear relationship between dose-tolerance and dose-rate providing an up to >110-fold increase in dose-tolerance [41, 42]. The dose rate for our data-collection was at $5*10^{12}$ ph/s (10 MGy/s), while the inverse dose-rate effect was even observed at $10^8$ ph/s, suggesting a more pronounced effect in our case. Consistent with the initial report, the inverse dose rate effect was later on demonstrated in a different study for a number of additional systems but with beam parameters highly comparable to ours. A clear lag-phase of >0.5 MGy was demonstrated for dose rates of ~1 MGy/s, where no loss of diffraction power can be observed [43]. Although these data were recorded comparably rapidly, the total data collection exceeded hundreds of milliseconds, while our data were collected within a short single 37 ms pulse. In combination with the ~10 times higher dose-rate we assume that the lag-phase for our experiment would exceed the 0.5 MGy value. In addition, the authors addressed the question of sample heating and found no significant increase in temperature, even for dose rates of ~25 MGy/s. In conclusion, previous experiments suggest that the dose-rates and cumulative doses applied in our work do not lead to major radiation damage. This is corroborated by our structural findings demonstrating equivalent electron density distributions for the different radiation doses.

**Biological implications**

Our previous studies have shown that the loss of order of the cap-domain loop is associated with the biological function of FAcD and is not induced by X-ray damage [2, 3]. We have determined several static, isomorphous structures, where both cap domains are present that support this finding (apo-structures collected on a home source – PDB-ID: 5T4T, on a synchrotron - PDB-ID: 3R41, and an SSX structure ablated by an IR-pulse – PDB-ID: 5NYV, respectively). In structures that were co-crystallized with various ligands the electron density for one or both cap domains is missing (measured on a home source - PDB-ID: 5K3F, 5K3E, 5K3B). In structures soaked with various ligands, one or both cap domains are missing (measured on home source and on a synchrotron beamline – PDB-ID: 3R3X, 3R3W, 3R3Y, 3R3V). Thus the increasing disorder in the cap-domain is indeed a mechanistic feature presenting during the catalytic cycle of FAcD. Consequently, we can observe the structural changes that are taking place during binding of the ligand and the subsequent increase in dynamics of the active site. The 752 ms time-point shows a Michaelis-complex (substrate

bound complex) of a catalytically active enzyme. In contrast, all previously described Michaelis complexes of FAcD were chemically trapped via a catalytically inactive mutant. However, in contrast to previous studies this time-resolved experiment investigates the wild-type enzyme at room temperature and hence reflects true snapshots of a '*molecular movie'* of the catalytic process.

**Outlook**

With the current limitation of available XFEL beamtime, the ability to conduct TR-SSX experiments at widely accessible synchrotron sources offers a major advantage to the structural biology community. Due to the current limitations in brightness of synchrotron sources, studies of nano-crystals or ultrafast time-scale structural dynamics still need to be conducted at XFELs. However, further increases in synchrotron brightness and improved detector technology promise to push this limit to the microsecond domain. Another possibility to increase the temporal resolution for time-resolved synchrotron crystallography includes a Hadamard Transformation based approach, which would also benefit from the technical setup described here [44]. Concordantly, the latter lays the groundwork to address questions about biological and enzymatic systems that could not be addressed previously. Its simplicity allows for easy transfer to other beamlines and requires little specialized training. Most importantly, currently the HARE approach offers the greatest versatility in addressing the biologically relevant timescales of enzymatic reactions in the millisecond to seconds time-scale.

## References


1. Sherrell, D.A. et al. A modular and compact portable mini-endstation for high-precision, high-speed fixed target serial crystallography at FEL and synchrotron sources. *Journal of Synchrotron Radiation* **22**, 1372-1378 (2015).
2. Chan, P.W., Yakunin, A.F., Edwards, E.A. & Pai, E.F. Mapping the reaction coordinates of enzymatic defluorination. *J Am Chem Soc* **133**, 7461-7468 (2011).
3. Kim, T.H. et al. The role of dimer asymmetry and protomer dynamics in enzyme catalysis. *Science* **355** (2017).
4. Moffat, K. Time-resolved crystallography. *Acta Crystallogr A* **54**, 833-841 (1998).
5. Moffat, K. Ultrafast time-resolved crystallography. *Nat Struct Biol* **5 Suppl**, 641-643 (1998).
6. Neutze, R. Opportunities and challenges for time-resolved studies of protein structural dynamics at X-ray free-electron lasers. *Philos Trans R Soc Lond B Biol Sci* **369**, 20130318 (2014).
7. Neutze, R. & Moffat, K. Time-resolved structural studies at synchrotrons and X-ray free electron lasers: opportunities and challenges. *Curr Opin Struct Biol* **22**, 651-659 (2012).
8. Gai, F., Hasson, K.C., McDonald, J.C. & Anfinrud, P.A. Chemical dynamics in proteins: the photoisomerization of retinal in bacteriorhodopsin. *Science* **279**, 1886-1891 (1998).
9. Westenhoff, S. et al. Time-resolved structural studies of protein reaction dynamics: a smorgasbord of X-ray approaches. *Acta Crystallogr A* **66**, 207-219 (2010).
10. Chavas, L.M., Gumprecht, L. & Chapman, H.N. Possibilities for serial femtosecond crystallography sample delivery at future light sources. *Struct Dyn* **2**, 041709 (2015).
11. DePonte, D.P. et al. Gas dynamic virtual nozzle for generation of microscopic droplet streams. *J Phys D Appl Phys* **41** (2008).
12. Fuller, F.D. et al. Drop-on-demand sample delivery for studying biocatalysts in action at X-ray free-electron lasers. *Nat Methods* **14**, 443-449 (2017).
13. Nelson, G. et al. Three-dimensional-printed gas dynamic virtual nozzles for x-ray laser sample delivery. *Opt Express* **24**, 11515-11530 (2016).
14. Oberthuer, D. et al. Double-flow focused liquid injector for efficient serial femtosecond crystallography. *Sci Rep* **7**, 44628 (2017).
15. Oghbaey, S. et al. Fixed target combined with spectral mapping: approaching 100% hit rates for serial crystallography. *Acta Crystallogr D Struct Biol* **72**, 944-955 (2016).
16. Owen, R.L. et al. Low-dose fixed-target serial synchrotron crystallography. *Acta Crystallographica Section D-Structural Biology* **73**, 373-378 (2017).
17. Roedig, P. et al. High-speed fixed-target serial virus crystallography. *Nat Methods* (2017).
18. Sierra, R.G. et al. Concentric-flow electrokinetic injector enables serial crystallography of ribosome and photosystem II. *Nat Methods* **13**, 59-62 (2016).
19. Weierstall, U. et al. Lipidic cubic phase injector facilitates membrane protein serial femtosecond crystallography. *Nat Commun* **5**, 3309 (2014).
20. Zarrine-Afsar, A. et al. Crystallography on a chip. *Acta Crystallogr D Biol Crystallogr* **68**, 321-323 (2012).
21. Boutet, S. et al. High-resolution protein structure determination by serial femtosecond crystallography. *Science* **337**, 362-364 (2012).
22. Chapman, H.N. et al. Femtosecond X-ray protein nanocrystallography. *Nature* **470**, 73-77 (2011).
23. Liu, W. et al. Serial femtosecond crystallography of G protein-coupled receptors. *Science* **342**, 1521-1524 (2013).
24. Redecke, L. et al. Natively inhibited Trypanosoma brucei cathepsin B structure determined by using an X-ray laser. *Science* **339**, 227-230 (2013).
25. Aquila, A. et al. Time-resolved protein nanocrystallography using an X-ray free-electron laser. *Optics Express* **20**, 2706-2716 (2012).
26. Arnlund, D. et al. Visualizing a protein quake with time-resolved X-ray scattering at a free-electron laser. *Nat Methods* **11**, 923-926 (2014).
27. Kupitz, C. et al. Serial time-resolved crystallography of photosystem II using a femtosecond X-ray laser. *Nature* **513**, 261-265 (2014).
28. Schotte, F. et al. Watching a signaling protein function in real time via 100-ps time-resolved Laue crystallography. *P Natl Acad Sci USA* **109**, 19256-19261 (2012).

29. Schotte, F. et al. Watching a protein as it functions with 150-ps time-resolved X-ray crystallography. *Science* **300**, 1944-1947 (2003).
30. Suga, M. et al. Light-induced structural changes and the site of O=O bond formation in PSII caught by XFEL. *Nature* **543**, 131-135 (2017).
31. Tenboer, J. et al. Time-resolved serial crystallography captures high-resolution intermediates of photoactive yellow protein. *Science* **346**, 1242-1246 (2014).
32. Beyerlein, K.R. et al. Mix-and-diffuse serial synchrotron crystallography. *IUCrJ* **4**, 769-777 (2017).
33. Olmos, J.L., Jr. et al. Enzyme intermediates captured "on the fly" by mix-and-inject serial crystallography. *BMC Biol* **16**, 59 (2018).
34. Stagno, J.R. et al. Structures of riboswitch RNA reaction states by mix-and-inject XFEL serial crystallography. *Nature* **541**, 242-246 (2017).
35. Neutze, R., Wouts, R., van der Spoel, D., Weckert, E. & Hajdu, J. Potential for biomolecular imaging with femtosecond X-ray pulses. *Nature* **406**, 752-757 (2000).
36. Fenwick, R.B., Esteban-Martin, S. & Salvatella, X. Understanding biomolecular motion, recognition, and allostery by use of conformational ensembles. *Eur Biophys J Biophy* **40**, 1339-1355 (2011).
37. Coppens, P. et al. The RATIO method for time-resolved Laue crystallography. *J Synchrotron Radiat* **16**, 226-230 (2009).
38. Garrett, B.C. et al. Role of water in electron-initiated processes and radical chemistry: issues and scientific advances. *Chem Rev* **105**, 355-390 (2005).
39. Owen, R.L., Rudino-Pinera, E. & Garman, E.F. Experimental determination of the radiation dose limit for cryocooled protein crystals. *Proc Natl Acad Sci U S A* **103**, 4912-4917 (2006).
40. Blake, C.C.F. & Phillips, D.C. in Biological Effects of Ionizing Radiation At the Molecular Level (Vienna; 1962).
41. Garman, E.F. Radiation damage in macromolecular crystallography: what is it and why should we care? *Acta Crystallogr D Biol Crystallogr* **66**, 339-351 (2010).
42. Southworth-Davies, R.J., Medina, M.A., Carmichael, I. & Garman, E.F. Observation of decreased radiation damage at higher dose rates in room temperature protein crystallography. *Structure* **15**, 1531-1541 (2007).
43. Owen, R.L. et al. Exploiting fast detectors to enter a new dimension in room-temperature crystallography. *Acta Crystallogr D Biol Crystallogr* **70**, 1248-1256 (2014).
44. Beddard, G.S. & Yorke, B.A. Pump-Probe Spectroscopy Using the Hadamard Transform. *Appl Spectrosc* **70**, 1292-1299 (2016).

# Supplementary Tables

## **Supplementary Table 1.** Data collection and refinement statistics.

| **Accession Code (Delay time)** | 6GXH (0 ms) | (6FSX) 30 ms | (6GXD) 752 ms | 6GXT (2,052 ms) | 6GXF (RadDam1) | 6GXL (RadDam2) |
|---|---|---|---|---|---|---|
| **Data collection** | | | | | | |
| Space group | $P2_1$ | $P2_1$ | $P2_1$ | $P2_1$ | $P2_1$ | $P2_1$ |
| Cell dimensions | | | | | | |
| *a*, *b*, *c* (Å) | 42.1 79.97 84.79 | 41.78, 79.38, 84.47 | 41.37, 78.54, 83.51 | 41.76, 79.54, 84.46 | 41.30, 78.56, 83.57 | 41.32, 78.54, 83.56 |
| α, β, γ (°) | 90.0, 102.9, 90.0 | 90.0, 102.9, 90.0 | 90.0, 102.8, 90.0 | 90.0, 102.9, 90.0 | 90.0, 102.9, 90.0 | 90.0, 102.9, 90.0 |
| Resolution (Å) | 86.13 - 1.80 (1.83 - 1.80) | 82.46 - 1.80 (1.83 - 1.80) | 81.50 - 1.80 (1.83 - 1.80) | 57.51 - 1.95 (2.00 - 1.95) | 81.42 - 1.80 (1.83 - 1.80) | 81.42 - 1.80 (1.83 - 1.80) |
| $CC_{1/2}$ | 96.7 (60.0) | 98.0 (86.4) | 90.1 (67.1) | 88.4 (55.7) | 74.74 (41.1) | 71.0 (39.6) |
| I/s (I) | 8.8 (3.7) | 11.1 (5.8) | 5.3 (3.3) | 4.0 (1.8) | 2.9 (2.1) | 3.0 (2.1) |
| Completeness (%) | 99.9 (99.9) | 100.0 (99.9) | 100 (100) | 99.9 (99.9) | 99.8 (99.4) | 99.9 (99.6) |
| Multiplicity | 132.2 (70.4) | 268.3 (200.3) | 39.5 (25.7) | 59.2 (45.7) | 9.2 (6.3) | 9.5 (6.5) |
| **Refinement** | | | | | | |
| Resolution range (Å) | 57.47-1.80 | 82.35-1.80 | 40.72-1.80 | 57.20-1.95 | 40.72-1.80 | 40.72-1.80 |
| No. reflections | 50455 | 49794 | 48304 | 39350 | 48165 | 48202 |
| $R_{work}$ (%) / $R_{free}$ (%) | 18.74 / 23.59 | 16.78 / 21.07 | 16.51 / 20.9 | 18.15 / 22.77 | 22.19 / 26.9 | 21.58 / 26.04 |
| *No. atoms* | | | | | | |
| Protein atoms | 4722 | 4786 | 4815 | 4756 | 4748 | 4748 |
| Ligand/ion | 0 | 2 | 7 | 10 | 0 | 0 |
| water | 261 | 246 | 443 | 186 | 412 | 412 |
| *B-factors* | | | | | | |
| protein | 25.93 | 22.94 | 21.12 | 27.87 | 21.14 | 24.5 |
| Ligand/ion | 0 | 43.55 | 26.69 | 26.47 | 0 | 0 |
| water | 33.06 | 34.33 | 34.16 | 34.91 | 32.31 | 32.68 |
| *R.m.s. deviations* | | | | | | |
| Bond length(Å) | 0.007 | 0.012 | 0.016 | 0.008 | 0.006 | 0.007 |
| Bond angles (°) | 0.864 | 1.293 | 1.55 | 0.905 | 0.82 | 0.927 |

Number of crystals (images) for earch structure is shown in Supplementary Table 2 * Values in parenthesis show the data in the outer resolution shell.

## **Supplementary Table 2.** Additional data collection and Ramachandran statistics

| **Delay time** | 0 ms | 30 ms | 752 ms | 2,052 ms | RadDam1 | RadDam2 |
|---|---|---|---|---|---|---|
| **Data collection** | | | | | | |
| Diffraction weighted dose per crystal (MGy) | 0.37 | 0.37 | 0.56 | 0.74 | 0.28 | 0.56 |
| Exposure time (s) | 0.037 | 0.037 | 0.015 | 0.037 | 0.015 | 0.015 |
| Energy (keV) | 12.7 | 12.7 | 12.1 | 12.7 | 12.1 | 12.1 |
| Flux (ph/s) | 5.00E+12 | 5.00E+12 | 1.00E+13 | 5.00E+12 | 1.00E+13 | 1.00E+13 |
| Beam size (µm) | 5 x 9 | 5 x 9 | 4 x 9 | 5 x 9 | 4 x 9 | 4 x 9 |
| Wavelength (Å) | 0.97626 | 0.97626 | 1.0089 | 0.97626 | 1.0089 | 1.0089 |
| Number of images included in scaling | 17128 | 23900 | 3318 | 5203 | 967 | 1008 |
| Wilson B-factor Å2 | 24.46 | 21.02 | 18.74 | 27.06 | 20.1 | 22.3 |
| Reflections observed | 6678211 (576427) | 13358810 (1605982) | 1910702 (200204) | 2330728 (288294) | 443142 (48861) | 458342 (50579) |
| Reflections unique | 50502 (8192) | 49797 (8019) | 48357 (7783) | 39351 (6312) | 48178 (7716) | 48210 (7733) |
| Reflections used for R-free | 2561 | 1630 | 2388 | 1863 | 2387 | 2389 |
| **Ramachandran statistics** | | | | | | |
| Favoured (%) | 97.12 | 96.77 | 97.47 | 97.12 | 96.13 | 96.3 |
| Allowed (%) | 2.88 | 2.89 | 2.36 | 2.71 | 3.37 | 3.03 |
| Outliers (%) | 0 | 0.34 | 0.17 | 0.17 | 0.51 | 0.67 |

* Values in parenthesis show the data in the outer resolution shell

# Supplementary Notes

## Synthesis of the photocaged Fluoroacetate (pHP-FAc)

### General Remarks

The melting point (m.p.) was measured on a Büchi M-560 apparatus in open capillaries. $^{1}$H NMR, $^{13}$C NMR, and $^{19}$F NMR spectra were recorded on Bruker AV III 400 and 500 spectrometers at 25 °C; chemical shifts ($\delta$) are reported in ppm using the residual solvent peak as reference. Atom to peak assignment was based on COSY, HSQC, and HMBC experiments. The infrared (IR) spectrum was recorded on a Perkin-Elmer Spectrum Two IR spectrometer, with the relative peaks intensities described as s (strong), m (medium) or w (weak), with br. (broad) if applicable. High-resolution electrospray ionization mass spectroscopy (HR-ESI-MS) was measured on a Bruker maXis spectrometer, and elemental analysis was measured with a LECO CHN/900 instrument.

### Reaction Scheme and Procedure

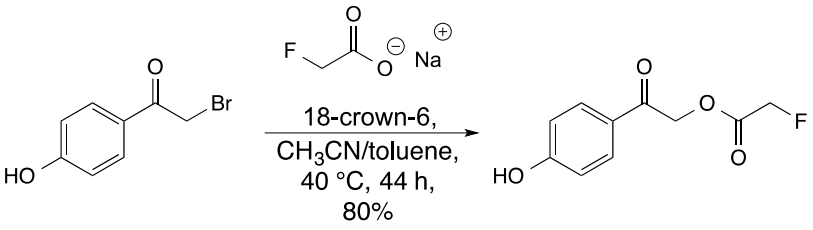


**Scheme S1.** Reaction for the preparation of photocaged fluoroacetate (pHP-FAc)

**2-(4-Hydroxyphenyl)-2-oxoethyl 2-fluoroacetate**

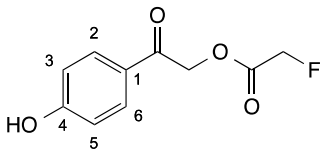

A solution of sodium 2-fluoroacetate (1.02 g, 10.23 mmol) in dry $CH_3CN$/toluene 1:1 (100 mL) under an Argon atmosphere was treated with 18-crown-6 (2.70 g, 10.23 mmol) and 2-bromo-1-(4-hydroxyphenyl)ethanone (2.00 g, 9.30 mmol), stirred at 40 °C for 44 h, and the solvents were evaporated. Purification by flash chromatography ($SiO_2$; $CH_2Cl_2$/MeOH gradient 100:0 to 98:2) gave the product (1.58 g, 80%) as white crystals.

$R_f$ = 0.23 ($SiO_2$; $CH_2Cl_2$/MeOH 99:1); m.p. 154–158 °C; $^1$H NMR (400 MHz, $CD_3OD$): $\delta$ = 5.08 (d, $J$ = 46.8 Hz, 2 H; $CH_2F$), 5.50 (s, 2 H; $CH_2O$), 6.85–6.92 (m, 2 H; H–C(3,5)), 7.82–7.93 ppm (m, 2 H; H–C(2,6)); $^{13}$C NMR (101 MHz, $CD_3OD$): $\delta$ = 67.48 (d, $^4J$(C,F) = 1.2 Hz; $CH_2O$), 78.62 (d, $^1J$(C,F) = 178.6 Hz; $CH_2F$), 116.58 (C(3,5)), 126.97 (C(1)), 131.54 (C(2,6)), 164.57 (C(4)), 169.39 (d, $^2J$(C,F) = 22.4 Hz; $CH_2FC$=O), 192.07 ppm ($OCH_2C$=O); $^{19}$F NMR (470 MHz, $CD_3OD$): $\delta$ = –233.20 ppm (t, $J$ = 46.7 Hz); IR (ATR): $\tilde{\nu}$ = 3205 (br., s), 2931 (w), 1771 (s), 1660 (m), 1576 (s), 1370 (m), 1206 (s), 1176 (s), 1078 (s), 962 (m), 841 (m), 698 cm$^{-1}$ (m); HR-ESI-MS: $m/z$ (%): 211.0410 (100, $[M - H]^-$, calcd for $C_{10}H_8FO_4^-$: 211.0412); elemental analysis calcd (%) for $C_{10}H_9FO_4$ (212.18): C 56.61, H 4.28, F 8.95; found: C 56.57, H 4.33, F 8.90.

**NMR spectra**

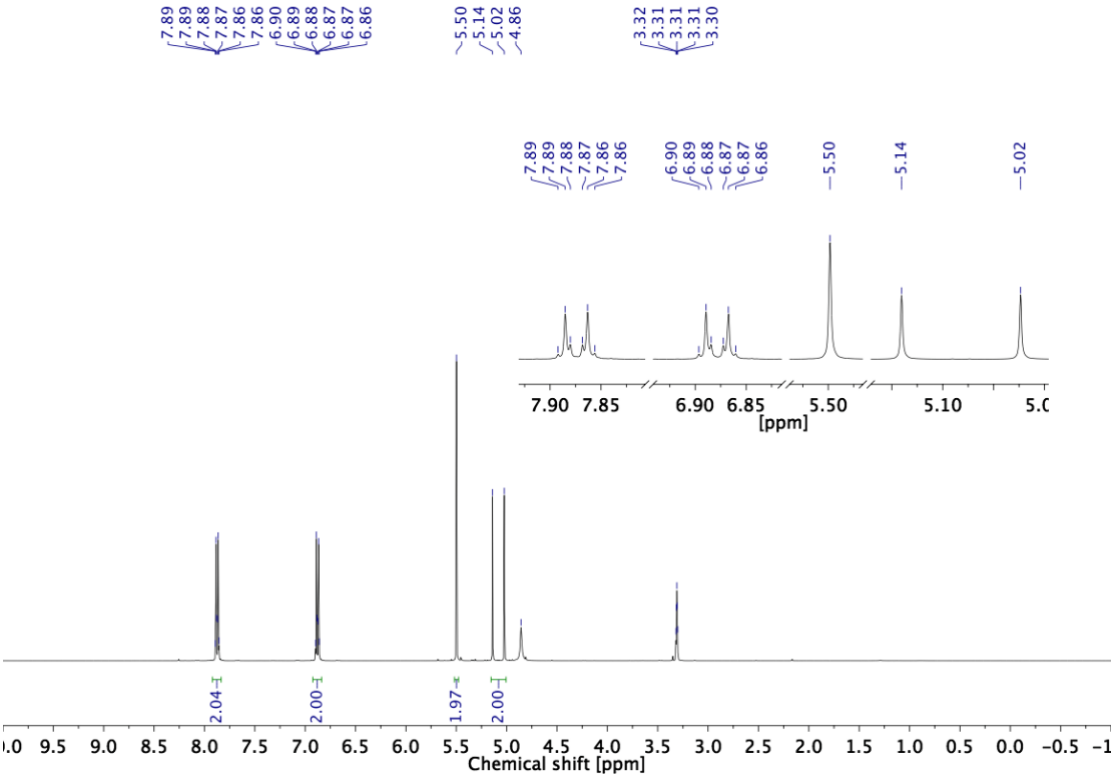


**Figure SN1:** $^1$H NMR (400 MHz, 298 K, $CD_3OD$).

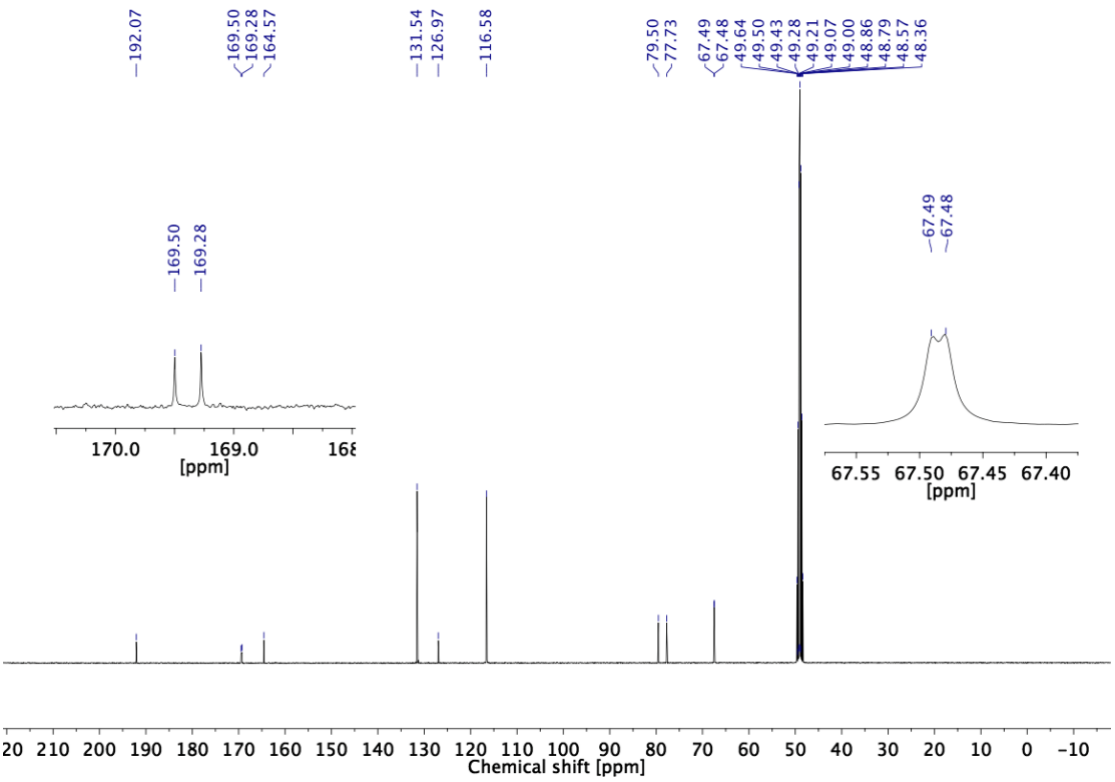


**Figure SN2:** $^{13}C$ NMR (101 MHz, 298 K, $CD_3OD$).

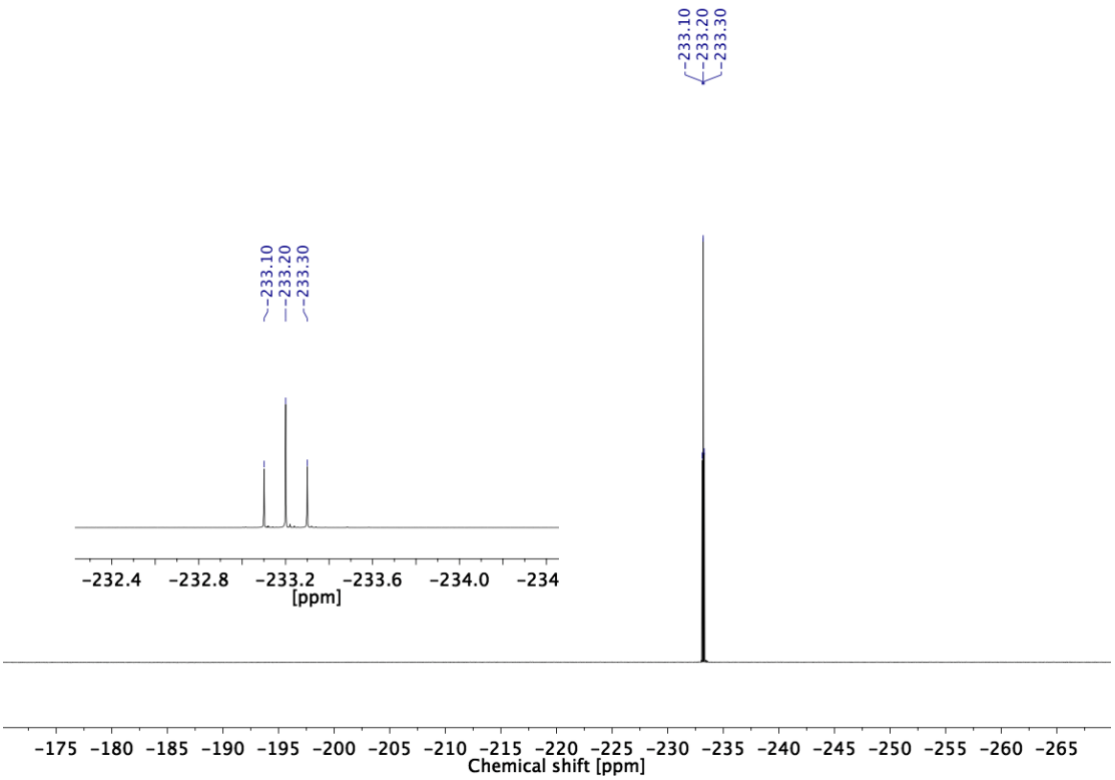


**Figure SN3:** $^{19}F$ NMR (470 MHz, 298 K, $CD_3OD$).